

Video Saliency Detection with Domain Adaption using Hierarchical Gradient Reversal Layers

G. Bellitto* · F. Proietto Salanitri* · S. Palazzo⁺ · F. Rundo · D. Giordano · C. Spampinato

Abstract In this work, we propose a 3D fully convolutional architecture for video saliency detection that employs multi-head supervision on intermediate maps (referred to as *conspicuity maps*) generated using features extracted at different abstraction level. More specifically, the model employs a single encoder and features extracted at different levels are then passed to multiple decoders aiming at predicting multiple saliency instances that are finally combined to obtain final output saliency maps. We also combine the hierarchical features extracted from the model's encoder with a domain adaptation approach based on gradient reversal at multiple scales in order to improve the generalization capabilities on datasets for which no annotations are provided during training. The results of our experiments on standard benchmarks, namely DHF1K, Hollywood2 and UCF Sports, show that the proposed model outperforms state-of-the-art methods on most metrics for supervised saliency prediction. Moreover, when tested in an unsupervised settings, it is able to obtain performance comparable to those achieved by supervised state-of-the-art methods.

Keywords Video Saliency Detection · Conspicuity Networks · Conspicuity maps · Domain Adaptation · Gradient Reversal Layer

G. Bellitto, F. Proietto Salanitri, S. Palazzo, D. Giordano, C. Spampinato
PeRCeiVe Lab - University of Catania
Tel.: +39-095-7387902
www.perceivelab.com

F. Rundo
STMicroelectronics, ADG Central R&D, Catania, Italy
* Contribute equally. ⁺ Corresponding author.

1 Introduction

Video saliency detection is the task of emulating human gaze fixation when perceiving dynamic scenes, and it is typically carried out by estimating spatio-temporal saliency maps from an input video sequence. Saliency detection, in general, can be seen as the upstream processing step of multiple applications that include object detection [13], behavior understanding [27, 30], video surveillance [26, 44, 14, 62] and video captioning [35, 53, 6]. Existing video saliency detection methods generally apply single-image saliency estimation on individual frames, and combine the results with recurrent layers to temporally model frame-level features. However, the two separate analysis stages in these models make them unable to fully capture spatio-temporal features simultaneously. Recently, 3D fully convolution models have been gained momentum to address this limitation by progressively aggregating spatio-temporal cues, achieving state-of-the-art performance on standard benchmarks. For example, TASED-Net [34] adopts a standard

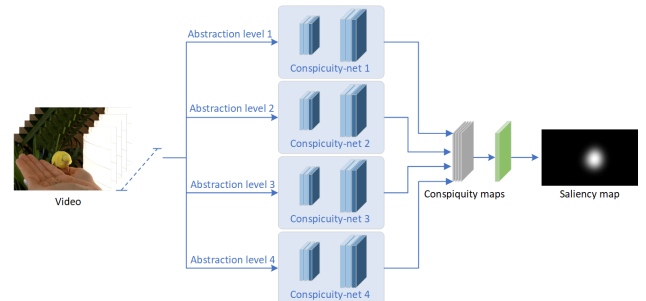


Fig. 1 SalGradNet overview

encoder-decoder architecture, as largely used in semantic segmentation tasks [42, 1, 36], that learns a compact spatio-temporal representation, and feeds it to a decoder

subnetwork to perform saliency prediction. While these models work well, saliency prediction is constrained by the aggregated representation learned at the model’s bottleneck, causing it to learn too task and dataset—specific representations that limit their generalization capabilities. Following the success of 3D convolutional architectures, in this paper we propose a model for video saliency prediction — SalGradNet — that, instead of using a compact spatio-temporal representation as in [34] for predicting visual saliency, generates multiple saliency maps by using features learned at different abstraction levels and then combines them in a multi-head supervision manner. We refer to the intermediate saliency maps as *conspicuity maps* as the employed architecture recalls the multi-scale model proposed in [17]. Using representations extracted at different abstraction levels (from shallow to deeper) allows the model to learn both generic (and more dataset-independent) and dataset-specific features obtaining the twofold objective to enhance the performance a specific dataset and to improve adaptation capabilities. Our approach takes inspiration from DVA [59], but extends it to the video domain by learning spatio-temporal cues for predicting visual saliency. More specifically, SalGradNet, shown in Fig. 1, is a 3D fully convolution network that employs an ensemble of multiple prediction models, each producing a *conspicuity-like* map at a specific abstraction level, for better saliency estimation.

As an additional contribution, we tackle the problem of generalization for video saliency detection. Indeed, state-of-the-art methods lack domain adaptation capabilities and require a mandatory fine-tuning step to perform well on datasets that they were not trained on. As the deep learning community is moving to build more generalizable models, we argue that this holds, even more so, for saliency detection research, given its fundamental nature in an artificial vision pipeline. To address this issue, our saliency detection network is provided with a multi-scale domain adaption mechanism, based on gradient reversal [10], that forces the model to learn *domain-independent* features. In particular, each abstraction level of SalGradNet is provided with a gradient reversal layer that prevent the learned representation from becoming dataset-specific.

We carry out extensive experiments testing SalGradNet on multiple video saliency benchmarks (DHF1K [55], UCF Sports [31, 46], Hollywood2 [32]) obtaining state-of-the-art performance and outperforming existing models. We also test the domain adaptation capabilities of SalGradNet to datasets for which no annotations were available during training. Our model shows remarkable results, achieving performance comparable to state-of-

the-art models that, instead, are trained (or fine-tuned) on those datasets in a standard supervised fashion.

2 Related work

Saliency detection has been long investigated in AI and computer vision research. In general, saliency models can be categorized in: *visual saliency prediction* approaches that attempt to predict the fixation points of a human observer; and *salient object detection* methods that, instead, focus on assessing the saliency of pixels w.r.t. objects of interest. Saliency detection methods can be further categorized according to whether they process still images (static saliency) or videos (dynamic saliency).

Static saliency detection has been researched for decades. Initial models, biologically-inspired [17] and employing hand-crafted features, were followed by recent CNN-based attempts [16, 38, 59] that yield superior performance, rapidly becoming state-of-the-art for static saliency detection. CNN-based static methods rely mainly on image classification models as backbone, and employ encoder-decoder architectures with different strategies to combine extracted features, from aggregation in a bottleneck to skip connection to deep supervision. Compared to saliency models for still images, saliency prediction in videos is an even more complex problem, due to the presence of the temporal dimension and to the additional computational effort it requires. Static saliency models have been adapted to dynamic saliency by using them in frame-by-frame mode, but these models are outperformed by the dynamic models that jointly process the temporal dimension. In recent years, a common strategy has been to extend static saliency models to the video scenario by incorporating motion features [57, 45, 48]. For example, [57] proposes a two-model architecture to exploit spatio-temporal features: the first module performs frame-level saliency prediction; the second module, instead, takes pairs of frames with saliency predicted by the first module, and generates a dynamic saliency map. [45] basically employs the same architecture as [57] and self-attention, through non-local operations [58]. SalEMA [28], instead, proposes a standard 2D encoder-decoder architecture, to which a recurrence module is added in the bottleneck to integrate temporal information provided by the previous frames.

Motion cues have been also included in saliency detection models through either recurrent neural networks applied to spatial feature encodings or convolutional recurrent networks. OM-CNN [19] is a dual-stream network that extracts spatial and temporal features using YOLO [41] and FlowNet [8], whose respective objectness

and motion features are then combined via a two-layer ConvLSTM. In ACLNet [55], the authors propose a similar strategy, where static saliency detection is provided by an attention module that perform a global spatial operation on learned features. These features are then given to a ConvLSTM to model temporal information. The recent SalSAC model [60], leveraging the success of self-attention for saliency prediction [7, 56], proposes an architecture with a shuffled attention mechanism on multi-level features for better modeling spatial saliency. Correlation features between multi-level features and shuffled attention on the same features are provided to a ConvLSTM for learning temporal cues.

With the recent availability of a large-scale saliency benchmark, i.e., DHF1K [55], 3D fully-convolutional models [3, 34], jointly extracting spatial and temporal features, have been proposed. RMDN [3] processes video clips with a 3D convolutional neural network based on C3D [50], and then employs LSTMs to enforce temporal consistency among the segments. TASED-Net [34] is a 3D fully-convolutional network, based on a standard encoder-decoder architecture, for video saliency detection without any additional feature processing steps. Similarly to the above approaches, our SalGradNet model is a 3D fully-convolutional network extending the multi-abstraction level analysis, proposed in [59] for static saliency, to the video domain by learning spatio-temporal cues. SalGradNet also performs domain adaption to generalize across datasets without the need to be fine-tuned. Indeed, in all prediction tasks, shifts in train and test distributions may lead to a significant degradation of the model’s performance. Trying to train a predictor capable of handling these shifts is commonly referred to as domain adaptation. Among the different domain adaption settings¹, we focus on *unsupervised* domain adaptation, which is the task of aligning features extracted from the model across source and target domains, without any labelled samples from the latter. Several techniques have been proposed, such as regularizing the maximum mean discrepancy [29], minimizing correlation [47], or adversarial discriminator accuracy [12, 51]. An effective approach to transfer the feature distribution from source to target domains is proposed in [11] through the use of Gradient Reversal Layer, treating domain invariance as a binary classification problem. This approach addresses domain adaptation by adversarially forcing a model to solve a given task while learning features that are non-discriminative across datasets. In SalGradNet we apply this strategy on multi-level features (unlike typical single-branch usage), in order to support the generalization of the saliency

prediction task to datasets for which no annotations are available during training. While unsupervised domain adaptation has been applied to image classification [52, 11], face recognition [20], object detection [49], semantic segmentation [64] and video action recognition [25] (among others), our work is, to our knowledge, the first to deal with domain adaptation on video saliency prediction. It is worthwhile to note that this is technically and fundamentally different from unsupervised saliency detection [63] that, instead, attempts to predict saliency by exploiting large unlabelled or weakly-labelled samples.

3 Method

3.1 Architecture overview

The proposed architecture is a fully-convolutional multi-branch encoder-decoder network for saliency prediction, illustrated in Fig. 2. An input sequence of consecutive video frames is first processed by a *feature extraction* path, which computes spatio-temporal features at different scales and abstraction levels. The extracted features serve as input to separate network branches that estimate a set of *conspicuity maps* at the corresponding points in the model, while at the same time providing skip paths to ease gradient flow during training. At the output of the model, conspicuity maps are combined to predict the saliency map for the last frame in the input sequence.

Our model is trained in a supervised way on a *source* dataset, for which saliency annotations are available. Additionally, each conspicuity subnetwork forks to a *domain classification* path, that is trained to classify whether an input video sequence (more precisely, the corresponding features at that abstraction level) is taken from the source domain or from a *target* domain, for which saliency annotations are not available and which cannot be employed for training through direct supervision. In order to perform adaptation between the source domain and the target domain, we apply the gradient reversal technique: the basic idea is to train the feature extraction layer, shared by the conspicuity networks and the domain classifiers, in an adversarial way, so the shared features computed by the model cannot be indicative of the input image’s domain. The goal of this approach is to force the model to learn features that are both discriminative and predictive — saliency-wise — as well as domain-invariant, in order to achieve satisfactory results even on the target domain, on which the model is not trained in a supervised way.

At inference time, saliency maps are predicted for each frame by applying the model in a sliding window fashion, as in [34]; the saliency map \mathbf{S}_t at time t is

¹ An extensive review of domain adaptation approaches is out of the scope of this paper and can be found in [40, 54]

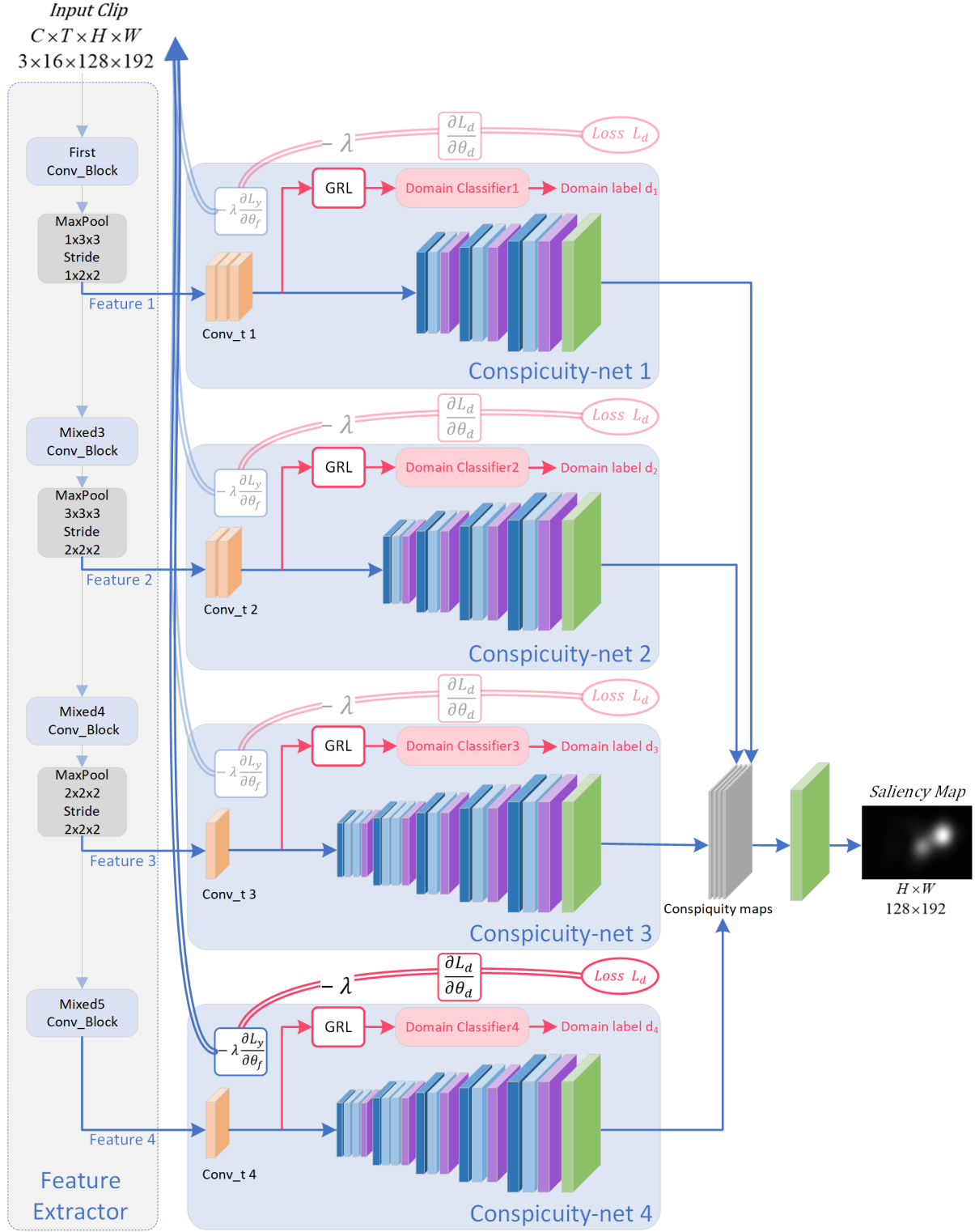


Fig. 2 A detailed illustration of our proposed SalGradNet architecture.

predicted from a sequence $\mathbf{V}_t = \{\mathbf{I}_{t-T+1}, \dots, \mathbf{I}_t\}$, where \mathbf{I}_t is the video frame at time t . To predict the first $T - 1$ frames, we reverse the chronological order of the

corresponding input clips: each \mathbf{S}_t for $1 \leq t \leq T - 1$ is predicted from the sequence $\mathbf{V}_t = \{\mathbf{I}_{t+T-1}, \dots, \mathbf{I}_t\}$.

In the following, we describe each of the components of our architecture. For brevity, detailed information on each layer in the model are provided in appendix A.

3.2 Feature extractor

The input to the model is a sequence of consecutive video frames, represented as a tensor of size $C \times T \times H \times W$, where C is the number of input channels (e.g., $C = 3$ for RGB frames), T is the length of an input sequence, and H and W define the spatial size of each frame. The first processing step of our model is a feature extractor that performs spatio-temporal encoding of the input sequence, and that employs S3D [61] as a backbone. The feature extractor is pre-trained on the Kinetics Dataset [21] for action recognition. The S3D backbone is a 3D convolutional neural network based on I3D [5], replacing 3D convolution with spatial and temporal separable 3D convolution: in detail, S3D replaces spatio-temporal $k_t \times k \times k$ filters with a cascade of a spatial $1 \times k \times k$ filter and a temporal $k_t \times 1 \times 1$, where k_t and k are the filter sizes in time and space, respectively. These operations are similar to depth-wise separable convolutions, but applied to the temporal dimension instead of the feature dimension. This architecture combines the advantages of spatio-temporal feature extraction with the higher computational efficiency and lower complexity of separable convolutions, yielding hierarchies of features that provide improved performance with respect to the I3D model from which it is inspired.

More in detail, our feature extractor receives an input video clip of $T = 16$ consecutive frames of size $H = 128$ and $W = 192$, and progressively reduces the dimensions of the feature maps through 3D max pooling to $2 \times 4 \times 6$ (time \times height \times width), while increasing the number of channels to 1024. However, in order to exploit the full potential of the learned hierarchical representations, we select feature maps at different levels of the extractor, corresponding to different abstraction details, in order to build a skip architecture able to capture multi-headed saliency responses. In our implementation, we select feature maps from the S3D backbone at the output of the second, third and fourth pooling layers and at the input of the last average pooling layer.

3.3 Conspicuity networks

As shown in previous works [59], both low and high-level features are important and complementary in the estimation of visual attention; for this reason, we design our architecture to process and fuse the multi-level information provided by the feature extractor. The idea

is to learn several *conspicuity maps* from the partial information produced at different levels of the feature extraction stack, thus pushing those feature maps to encode saliency-relevant information from the very first layers of the model.

Each conspicuity network in the model processes one of the spatio-temporal feature blocks extracted from the previous module and returns a single-channel saliency map, encoding the conspicuity of spatial locations at that level of abstraction. In detail, since each subnetwork predicts a single saliency map corresponding to the last frame in the input video sequence, the temporal dimension is gradually removed from the input feature maps, by applying a cascade of spatially point-wise convolutions (i.e., with kernel $3 \times 1 \times 1$ and stride $2 \times 1 \times 1$) that halve the temporal dimension at each step. The number of needed point-wise convolutions varies for each conspicuity network, depending on the size of the input feature maps.

After that, the (now purely spatial) set of feature maps is processed by a stack of 2D convolutional layers, interleaved with bilinear upsampling blocks, each of which doubles the spatial size of the feature maps until the original resolution of each frame is recovered.

3.4 Saliency prediction

The four conspicuity maps produced by the above subnetworks are also combined to produce the saliency map for the last frame of the input sequence. In detail, we concatenate the conspicuity maps into a $4 \times 128 \times 192$ tensor (channels \times height \times width). Conspicuity information at each spatial location of the above tensor is locally combined by means of a pixel-wise convolution with logistic activation into a single-channel saliency map, that is the final prediction of the model.

At training time, the whole model (feature extractor, conspicuity networks and saliency predictor) is trained supervisedly on the source dataset in order to minimize the Kullback-Leibler (KL) divergence, which has shown to perform well in saliency tasks [34, 16], between the predicted saliency map and conspicuity maps, and the correct target. It should be noted that computing KL loss for the maps generated by the conspicuity networks is significantly different from the concept of deep supervision, as instead claimed in [59], since the predictions are not done at different network’s depths, but all at the same level with different abstraction information. This means that the maps generated by the model’s branches do not encode coarse to fine saliency information, rather they are meant to assess global saliency using different set of features: from the most generic ones (in the shallow layers) to the most dataset-specific ones (in the deeper

layers) This explains why we opt for referring to each branch as conspicuity network given the architectural resemblance to the hierarchical biologically-inspired model proposed in [23]. More formally, given the predicted output saliency map \mathbf{S}_t , the four conspicuity maps $\mathbf{C}_{t,i}$ with $i = 1, 2, 3, 4$ and the ground-truth map \mathbf{G}_t for a given target frame, our *multi-head saliency loss* \mathcal{L}_s is computed as follows :

$$\mathcal{L}_s(\mathbf{S}_t, \mathbf{C}_t, \mathbf{G}_t) = \sum_{j=1}^4 \sum_i G_{t,i} \log \frac{G_{t,i}}{C_{t,j,i}} + \sum_i G_{t,i} \log \frac{G_{t,i}}{S_{t,i}} \quad (1)$$

where index i iterates over all pixels, index j iterates over the four conspicuity maps, $G_{t,i}$, $S_{t,i}$ and $C_{t,i,j}$ are corresponding pixels of, respectively, the ground truth map, the output saliency map and the j -th conspicuity map .

3.5 Domain adaptation

In addition to training the model in a supervised way on the source domain, we also encourage the feature extractor to generalize over the target domain, on which no saliency annotation is available. Unsupervised domain adaptation [11] is carried out by training a domain classifier to distinguish between features of the source domain from features computed from videos domain, while at the same time training the feature extractor to *maximize* the domain classification loss. This approach can be implemented by training the classifier in a standard way, i.e., by minimizing the negative log-likelihood loss, and inserting a *gradient reversal layer* (GRL) at the output of the layer whose features should be adapted and right before the domain classifier, so that model parameters before that point are updated towards the direction of *increasing* classification loss, while the classifier is still updated to minimize its own error.

A gradient reversal layer has no associated parameters and can be simply implemented as a layer that changes the sign of the gradient w.r.t. loss that it receives from the following layer, before backpropagating it to the previous layer, optionally scaling it by a λ parameter.

In our model, we integrate domain adaptation by inserting, in all of the conspicuity subnetworks, a branch with a gradient reversal layer and a domain classifier after the temporal-dimension removal layer (see Fig. 2). More formally and generally, given an input video clip \mathbf{V}_t with associate binary domain label $d \in \{0, 1\}$ (source or target, respectively), we compute a set of associated

domain classification losses $\{\mathcal{L}_{d,1}, \dots, \mathcal{L}_{d,C}\}$ from C domain classifiers attached to the conspicuity networks. If we indicate by \hat{d}_i the probability of the input being from the target domain estimated by the i -th classifier, the corresponding negative log-likelihood loss is defined as:

$$\mathcal{L}_{d,i}(d, \hat{d}_i) = -d \log \hat{d}_i - (1 - d) \log (1 - \hat{d}_i) \quad (2)$$

The overall loss for domain classification is simply computed as the sum of the individual contributions, since the interaction between saliency prediction and domain adaptation is controlled by the λ hyperparameter in the gradient reversal layers:

$$\mathcal{L}_d = \sum_{i=1}^C \mathcal{L}_{d,i} \quad (3)$$

During training, we alternately pass a batch of videos from the source domain and a batch of videos from the target domain: on the former, we compute and backpropagate both the saliency prediction loss \mathcal{L}_s and the domain classification loss \mathcal{L}_d (with target $d = 0$); on the latter, we can only compute and backpropagate the domain classification loss \mathcal{L}_d (with target $d = 1$), since no saliency annotation is available on the target domain. Minimizing the domain classification loss has the effect to train the classifiers to better discriminate between the source and the target domains, while at the same time adversarially training the feature extractor (and the initial temporal-removal layers in the conspicuity networks) to produce features that confuse the classifier, and hence that are domain-independent.

Architecturally, each domain classifier consists of a stack of 1×1 spatial convolutions aimed at reducing the number of features, followed by fully-connected layers, the last of which provides binary classification prediction of the input video's domain.

The presence of the gradient reversal layer ensures that the distribution at the output of the feature extractor block is similar for the target and source domains, while being at the same time informative for the saliency prediction task.

4 Experimental Results

4.1 Datasets

In this section we review the datasets used in our experiments:

- **DHF1K** [55] consists of 1,000 high-quality videos with a large diversity of scenes, objects, types of motion, complexity of backgrounds; the length of

the videos varies between 186 and 1558 frames, for a total of around 600,000 frames, each annotated with fixation points from 17 observers. The dataset is split into 600/100/300 videos for training, validation and test sets, respectively. The training set contains about 350,000 frames. While the annotations for train and validation sets are available, test annotations are not released. The dataset curators run the benchmark web platform where the results of the saliency networks on the test set are published.

- **LEDOV** [18]: a large-scale eye tracking dataset including 538 videos and 179,336 frames in total. It provides videos of daily action, sports, social activity and art performance. These videos are selected from different publicly available sources. Following the original indication of the author, the dataset is divided into 461 videos for training, 36 videos for validation, and the remain 41 for test. Eye gaze data from 32 participants are acquired using a Tobii TX300 eye tracker.
- **UCF Sports** [31] contains 150 videos taken from the UCF Sport Action Dataset [46]. This dataset was initially designed for action recognition, with human gaze annotations collected later. Videos are selected from broadcast television channels such as the BBC and ESPN, and they include 10 actions, such as diving, swinging, walking, horse riding, skateboarding, etc. Fixations are collected from 16 subjects, who had been directed towards a task-driven observation, since they had to identify the action that occurred in the video. The dataset is split into 103 videos for training, and the remaining 47 for test, for a total of around 6,500 frames for training and 3,000 frames for test. The length of the videos varies between 20 and 140 frames.
- **Hollywood2** [33]: this dataset contains 6,659 video sequences and derives, like UCF Sports, from a dataset for action recognition [31]. The videos are collected from 69 Hollywood movies divided into 33 training movies and 36 test movies, with 12 categories of actions, such as eating, driving a car, answering the phone, kissing, running. Eye gaze data are collected from 19 subjects. Although it is a very large dataset, its content is limited to human actions in movie scenes and, as for UCF Sports, the annotations are collected in a task-driven way. The whole set of videos is split into 3,100 clips for training and 3,559 clips for testing; most of them are shorter than 16 frames, which represents the minimum length for a clip to be employed by our model. However, as commonly done in other works [9, 34] we only use a subset of these two splits, discarding all clips that are shorter than 16 frames: we use 1,904 clips for

training, and 2,373 for testing, for a total of around 210,000 and 236,000 frames, respectively.

Fig. 3 provides some statistics about the training splits of the datasets employed for supervised learning of video saliency: 1) UCF Sports is the smallest one in terms of available videos and average number of frames per video, thus it seems to be unsuitable for models with high capacity as they likely overfit it; 2) Hollywood2, instead, contains the highest number of videos but the majority has a very short number of frames (see the bottom-right histogram in Fig. 3), thus it may disadvantage methods modelling temporal cues; 3) DHF1K appears to be the most balanced in terms of videos and number of frames per videos.

4.2 Training procedure

In our experiments, the S3D backbone is pre-trained on Kinetics400 [21]. After evaluating different training approaches and different hyperparameter configurations in order to find the best combination, the networks are trained for 2500 iterations, using Adam as optimizer [22] with learning rate of 10^{-3} and weight decay of 2×10^{-7} . The λ parameter of the gradient reversal layers during training gradually varies from 0 to 1:

$$\lambda = \frac{2}{1 + e^{-10 \cdot p}} - 1 \quad (4)$$

where p linearly goes from 0 to 1 according to the formula:

$$p = \frac{\text{current_iteration}}{\text{total_iterations}} \quad (5)$$

During training, sequences of $T = 16$ consecutive frames are randomly sampled from the dataset’s videos, and each frame is spatially resized to 128×192 . We employed a batch size of 200, although for memory limitations we forward batches of 8 samples at each time, which accumulating gradients and updating the model’s parameters every 25 such forward steps. For practical purposes (e.g. see Eq. 5), each “iteration” consists in processing a full batch of 200 samples. When training with domain adaptation, we also forward a batch of samples from the source domain and one of samples from the target domain, and use them to update the domain classifier only.

To evaluate performance, we use each dataset’s own training/test split when available, with 10% of the training data used as validation split. An exception is represented by DHF1K, since ground-truth annotations for the test set are not provided for blind assessment: in this case, when comparing to state-of-the-art methods

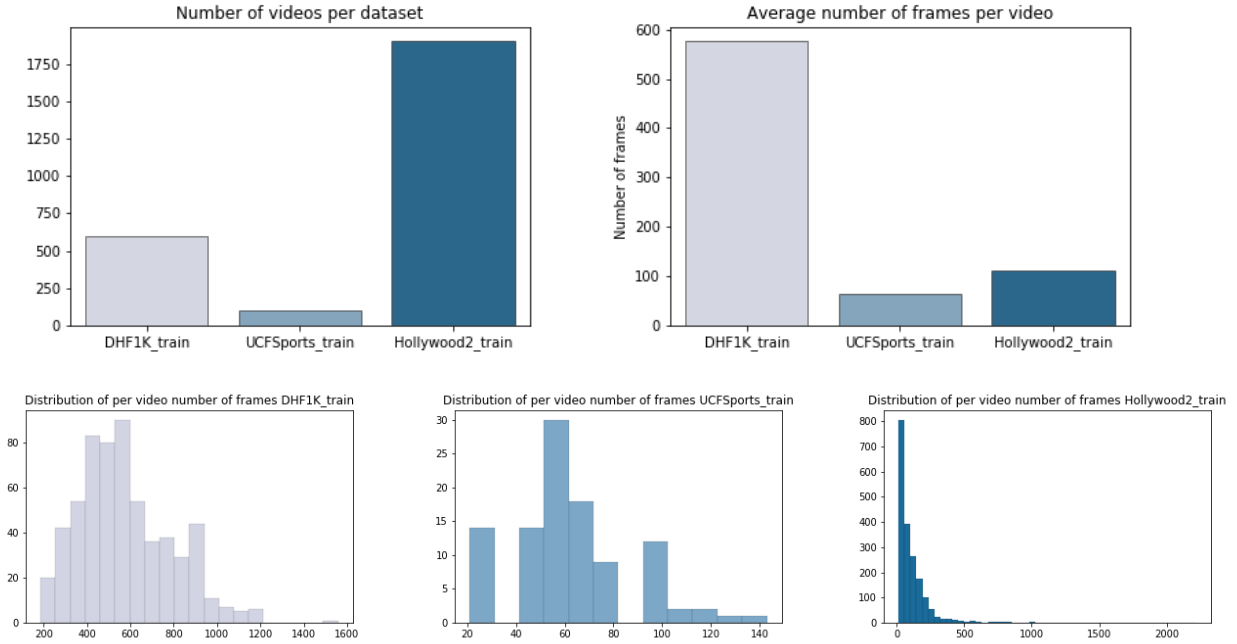


Fig. 3 Statistics of the training sets of DHF1K, Hollywood and UCF Sports.

(Tab. 1), we report the test accuracy as computed by the dataset curators; when internally comparing our model with and without domain adaptation (Tab. 3 to 7), we employ the original validation set as test set, due to the large number of experiments and to the time required for obtaining performance metrics on the curators’ test set (about five days).

Every 100 iterations a validation step is performed: the model processes all videos in the dataset’s validation set in sliding-window fashion. For inference on the test set, we employ the model’s parameters that yielded the best validation accuracy.

To compare the results obtained by the models, we use five commonly used evaluation metrics for video saliency prediction: Normalized Scanpath Saliency (NSS), Linear Correlation Coefficient (CC), Area under the Curve by Judd (AUC-J), Shuffled-AUC (s-AUC) and Similarity (SIM). An extensive review of these metrics can be found in [4]. Higher scores on each metric mean better performance.

4.3 Video saliency detection performance

We first test the performance of our model in the supervised scenario (i.e., without enabling the domain adaptation branches) on the DHF1K test benchmark, to evaluate its capabilities in the saliency prediction task. Tab. 1 shows the performance of our approach compared to the state of the art. SalGradNet, without domain

adaptation (referred in Table 1 to as $\text{SalGradNet}_{w/o \text{ DA}}$), outperforms all state-of-the-art methods on two out of five metrics (AUC-J, CC), while obtaining the second best values in two other metrics (NSS, s-AUC) and the third best value in the remaining metric (SIM). In particular, $\text{SalGradNet}_{w/o \text{ DA}}$ outperforms on four out of five metrics UNISAL [9], which is currently ranked first in the DHF1K competition available at <https://mmcheng.net/videosal/>. However, this comparison deserves an additional discussion. UNISAL [9] is characterized by using MobileNetV2 [43] as backbone and employing recurrent connections; most importantly, UNISAL, unlike to our model, is designed to be very dataset-oriented, with several layers that perform dataset-specific operations, while our approach is completely dataset-agnostic. Moreover, UNISAL employs spatial priors (even those, dataset-specific), limiting its generalization capabilities to new unseen data. In our work, we instead choose not to use priors at all, since we believe that the performance gain that is obtained by using priors is only related to biases in most common datasets, thus reducing the generalization capabilities of a model when employed in an uncontrolled scenario or where no human operator controls the camera’s field of view. Excluding UNISAL from the comparison, SalGradNet outperforms by large margin, on all the five employed metrics, the second-best method, i.e., SalSAC [60]. Comparing SalGradNet with TASED-Net [34], which also employs S3D [61] as backbone, it is possible to notice that SalGradNet significantly outperforms TASED-Net in almost all metrics

using only half of the frames employed by TASED-Net (16 versus 32). TASED-Net slightly outperforms SalGradNet only on s-AUC, a metric that is unaffected by center bias and that measures performance at the peripheral areas of the image, where a larger temporal context may allow to better capture the motion of an object. The better performance obtained by our method w.r.t TASED-Net [34] demonstrates that using the conspicuity networks indeed is useful to achieve more accurate saliency assessment.

| | NSS | CC | SIM | AUC-J | s-AUC |
|------------------------------|--------------|--------------|--------------|--------------|--------------|
| GBVS [15] | 1.474 | 0.283 | 0.186 | 0.828 | 0.554 |
| STSCovNet [2] | 1.632 | 0.325 | 0.197 | 0.834 | 0.581 |
| Deep Net [39] | 1.775 | 0.331 | 0.201 | 0.855 | 0.592 |
| SALICON [16] | 1.901 | 0.327 | 0.232 | 0.857 | 0.590 |
| OM-CNN [19] | 1.911 | 0.344 | 0.256 | 0.856 | 0.583 |
| DVA [59] | 2.013 | 0.358 | 0.262 | 0.860 | 0.595 |
| SalGAN [37] | 2.043 | 0.370 | 0.262 | 0.866 | 0.709 |
| ACLNet [55] | 2.354 | 0.434 | 0.315 | 0.890 | 0.601 |
| SalEMA [28] | 2.574 | 0.449 | 0.466 | 0.890 | 0.667 |
| STRA-Net [24] | 2.558 | 0.458 | 0.355 | 0.895 | 0.663 |
| TASED-Net [34] | 2.667 | 0.470 | 0.361 | 0.895 | 0.712 |
| SalSAC [60] | 2.673 | 0.479 | 0.357 | 0.896 | 0.697 |
| UNISAL [9] | 2.776 | 0.490 | 0.390 | 0.901 | 0.691 |
| Ours_{w/o} DA | 2.747 | 0.499 | 0.395 | 0.903 | 0.703 |

Table 1 Comparison of SalGradNet with other state-of-the-art methods on the test set of DHF1K. **Ours_{w/o} DA** (i.e., SalGradNet without domain adaptation) outperforms all state-of-the-art methods on two out of five metrics (AUC-J, CC), while obtaining the second best values in two other metrics (NSS, SIM) and the third best value in the remaining metric (s-AUC).

We also test our model on Hollywood2 and UCF Sports to prove the effectiveness of the solutions adopted. In these cases, we use our model pre-trained on DHF1K, then fine-tuned on each specific dataset. The results are reported in Table 2 showing that our model achieves a good generalization capability, as it ranks among the three best methods. The different performance behavior of our model when tested on DHF1K (where it ranked first) and on Hollywood2 and UCF sports lies in the nature of these datasets. Indeed, both Hollywood2 and UCF sports are task-oriented saliency benchmarks, while DHF1K is a free-viewing one: this suggests that in Hollywood2 and UCF sports, saliency maps are more concentrated towards the objects of interest, while in DHF1K saliency maps are more spread across the video sequences, as also observed in [9]. Moreover, UCF sports is a much smaller dataset than DHF1K, leading to a quicker overfitting of our model, and Hollywood2 contains shorter video sequences than DHF1K, thus reducing the impact that spatio-temporal cues may have on

saliency prediction. An overview of the dataset statistics confirming these claims is provided in the previous section and shown in Fig. 3.

| Hollywood2 test | | | | |
|------------------------------|--------------|--------------|--------------|--------------|
| Method | AUC-J | SIM | CC | NSS |
| SALICON | 0.856 | 0.321 | 0.425 | 2.013 |
| DVA | 0.886 | 0.372 | 0.482 | 2.459 |
| ACLNet | 0.913 | 0.542 | 0.623 | 3.086 |
| SalEMA | 0.919 | 0.487 | 0.613 | 3.186 |
| STRA-Net | 0.923 | 0.536 | 0.662 | 3.478 |
| TASED-Net | 0.918 | 0.507 | 0.646 | 3.302 |
| SalSAC | 0.931 | 0.529 | 0.670 | 3.356 |
| UNISAL | 0.934 | 0.542 | 0.673 | 3.901 |
| Ours_{w/o} DA | 0.927 | 0.558 | 0.668 | 3.426 |
| UCF Sports test | | | | |
| Method | AUC-J | SIM | CC | NSS |
| SALICON | 0.848 | 0.304 | 0.375 | 1.838 |
| DVA | 0.872 | 0.339 | 0.439 | 2.311 |
| ACLNet | 0.897 | 0.406 | 0.510 | 2.567 |
| SalEMA | 0.906 | 0.431 | 0.544 | 2.638 |
| STRA-Net | 0.910 | 0.479 | 0.593 | 3.018 |
| TASED-Net | 0.899 | 0.469 | 0.582 | 2.920 |
| SalSAC | 0.926 | 0.534 | 0.671 | 3.523 |
| UNISAL | 0.918 | 0.523 | 0.644 | 3.381 |
| Ours_{w/o} DA | 0.913 | 0.493 | 0.594 | 3.001 |

Table 2 Comparison of SalGradNet with other state-of-the-art method on Hollywood2 and UCF Sports datasets. In bold the best results, in italics the second-best results.

4.4 Domain adaption performance

To assess the performance of our hierarchical domain adaptation approach, we run experiments selecting different combinations of datasets to be used as source domain (used in a supervised way during training), target domain (used in an unsupervised way during training) and test dataset (never seen during training). During these experiments, the models with both GRL and without domain adaption are trained in parallel by providing the same input sequence to avoid any evaluation bias.

Tab. 3-7 show the results of our experiments, reporting the performance achieved by our model when not performing domain adaptation (as described in the previous section) and when integrating the gradient reversal branches at each conspicuity subnetwork.

Based on our experiments, two main patterns of results can be identified, depending on whether DHF1K is employed as source domain and not.

In the first case (see Tab. 3, 4 and 5), it can be noticed that the employment of gradient reversal layers consistently improves performance over all test datasets, compared to the base model that is simply trained on

the source dataset. It is interesting to highlight that this improvement is noticeable both when the test dataset is different from the source and target datasets (i.e., never seen during training, in either supervised or unsupervised way) and when the test dataset is DHF1K itself. This shows that domain adaptation can also act as a regularization objective to encourage the model to learn more general features, see Fig. 4. Furthermore, when using LEDOV as target dataset for domain adaptation, the performance gain is higher than the one with UCF Sports and Hollywood2 as target datasets, and this is due again to the characteristics of these two datasets (less scene variability and shorter video duration than in LEDOV) that limit the regularization effects obtained by the hierarchical gradient reversal layers. Despite the results shown in Table 1 and Table 3 are obtained with different DHF1K dataset splits (i.e., the former reports the results on the DHF1K test split while the latter on the validation split using the training procedure described in Sect. 4.2), it can be noticed that our approach empowered with hierarchical GRL yields performance comparable to those of the state of the art methods while trained supervisedly.

When DHF1K is employed as target domain (see Tab. 6 and 7), the use of gradient reversal layers degrades performance. A possible interpretation of this discrepancy can be attributed to the specific characteristics of Hollywood2 and UCF Sports, as already mentioned in the previous section. Indeed, the limited variability of spatio-temporal features from videos in Hollywood2, as shown by the significantly shorter duration of videos reported in Fig. 3, may be the cause of why it becomes harder for the model to move clustered features and allow for learning more general representations. Similarly, when UCF Sports is used as source domain, the small size of the dataset makes it easier for the model to focus on the supervised saliency prediction task (on which it can easily achieve a low training loss), rather than minimizing the domain adaptation loss.

5 Ablation Studies

To validate the importance and effectiveness of the design choices made for the design and training of the network, we explore some model variants (without domain adaptation) on the validation set of the DHF1K:

1. We first investigate how the number of video frames fed into the model affects the performance. Due to the hardware architecture used, it is not possible to try with a frame number greater than $T = 16$; therefore, we compute the results with $T = 8$ and $T = 16$ number of frames as input to the model.

| source: DHF1K - target: LEDOV → testing on DHF1K | | | | |
|--|--------------|--------------|--------------|--------------|
| Model | AUC-J | NSS | CC | SIM |
| No GRL | 0.903 | 2.685 | 0.483 | 0.364 |
| GRL | 0.906 | 2.715 | 0.486 | 0.365 |
| source: DHF1K - target: LEDOV → testing on UCF Sports | | | | |
| Model | AUC-J | NSS | CC | SIM |
| No GRL | 0.889 | 2.494 | 0.536 | 0.442 |
| GRL | 0.900 | 2.584 | 0.555 | 0.452 |
| source: DHF1K - target: LEDOV → testing on Hollywood2 | | | | |
| Model | AUC-J | NSS | CC | SIM |
| No GRL | 0.922 | 3.011 | 0.622 | 0.502 |
| GRL | 0.926 | 3.066 | 0.623 | 0.505 |

Table 3 Domain adaptation with source: DHF1K, target: LEDOV; evaluation on DHF1K, UCF Sports and Hollywood2. Best results in bold.

| source: DHF1K - target: UCF Sports → testing on DHF1K | | | | |
|---|--------------|--------------|--------------|--------------|
| Model | AUC-J | NSS | CC | SIM |
| No GRL | 0.905 | 2.724 | 0.489 | 0.370 |
| GRL | 0.904 | 2.727 | 0.489 | 0.373 |
| source: DHF1K - target: UCF Sports → testing on UCF Sports | | | | |
| Model | AUC-J | NSS | CC | SIM |
| No GRL | 0.880 | 2.483 | 0.537 | 0.442 |
| GRL | 0.893 | 2.514 | 0.539 | 0.448 |
| source: DHF1K - target: UCF Sports → testing on Hollywood2 | | | | |
| Model | AUC-J | NSS | CC | SIM |
| No GRL | 0.925 | 3.020 | 0.621 | 0.501 |
| GRL | 0.925 | 3.104 | 0.626 | 0.511 |

Table 4 Domain adaptation with source: DHF1K, target: UCF Sports; evaluation on DHF1K, UCF Sports and Hollywood2. Best results in bold.

2. As for the conspicuity networks, we evaluate the performance of our network in different configurations, adding the different Conspicuity-Nets one at a time, without domain adaptation and, at this stage, without multi-head loss.
3. Finally, we evaluate the performance of our full model when applying the multi-head loss on all conspicuity maps.

Thus, the *Baseline* configuration refers to the network in a simple encoder-decoder configuration, i.e., without the conspicuity maps and multi-head loss. More specifically, in the baseline model, the feature extractor remains unchanged, but only the final feature map is

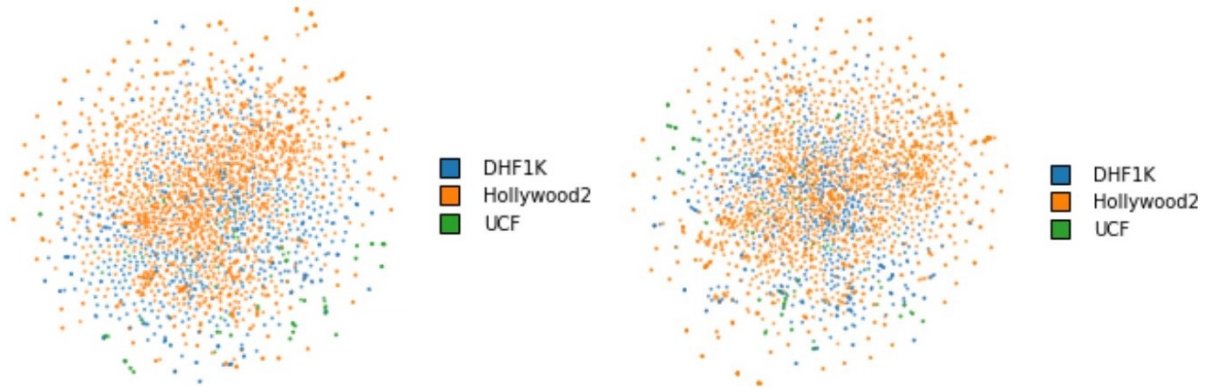


Fig. 4 Effect of GRL on dataset features. *t*-SNE visualization of the features extracted at the end of the Feature Extractor (Feature 4 in Fig. 2) of SalGradNet when trained it without GRL (left image) and with GRL (right image). Source dataset: DHF1K, target dataset: LEDOV. When using multi-scale GRL, learned features across dataset become more spread out leading to better generalization capabilities.

| source:DHF1K - target: Hollywood2 → testing on DHF1K | | | | |
|---|--------------|--------------|--------------|--------------|
| Model | AUC-J | NSS | CC | SIM |
| No GRL | 0.905 | 2.700 | 0.484 | 0.367 |
| GRL | 0.905 | 2.737 | 0.483 | 0.370 |
| source: DHF1K - target: Hollywood2 → testing on UCF Sports | | | | |
| Model | AUC-J | NSS | CC | SIM |
| No GRL | 0.896 | 2.522 | 0.543 | 0.440 |
| GRL | 0.893 | 2.534 | 0.542 | 0.444 |
| source: DHF1K - target: Hollywood2 → testing on Hollywood2 | | | | |
| Model | AUC-J | NSS | CC | SIM |
| No GRL | 0.925 | 3.062 | 0.624 | 0.504 |
| GRL | 0.925 | 3.101 | 0.632 | 0.510 |

Table 5 Domain adaptation with source: DHF1K, target: Hollywood2; evaluation on DHF1K, UCF Sports and Hollywood2. Best results in bold.

| source: UCF Sports - target: DHF1K → testing on UCF Sports | | | | |
|---|--------------|--------------|--------------|--------------|
| Model | AUC-J | NSS | CC | SIM |
| No GRL | 0.901 | 2.803 | 0.588 | 0.489 |
| GRL | 0.905 | 2.756 | 0.579 | 0.478 |
| source: UCF Sports - target: DHF1K → testing on DHF1K | | | | |
| Model | AUC-J | NSS | CC | SIM |
| No GRL | 0.880 | 2.237 | 0.405 | 0.325 |
| GRL | 0.877 | 2.160 | 0.392 | 0.309 |
| source: UCF Sports - target: DHF1K → testing on Hollywood2 | | | | |
| Model | AUC-J | NSS | CC | SIM |
| No GRL | 0.899 | 2.468 | 0.517 | 0.433 |
| GRL | 0.899 | 2.427 | 0.509 | 0.423 |

Table 6 Domain adaptation with source: UCF Sports, target: DHF1K; evaluation on UCF Sports, DHF1K and Hollywood2. Best results in bold.

used. Subsequently, the extracted features are given as input to a temporal convolution to reduce the temporal dimension to 1 and then the prediction is computed using a 2D decoder. The temporal convolution and the decoder are identical to those of the Conspicuity-net 4.

The model variants and their performance (computed on the DHF1K validation set) are reported in Table 8. The results show that: a) more input frames yields better prediction accuracy; b) each conspicuity net makes its own contribution to improving the final performance; c) multi-head loss on conspicuity maps slightly enhances saliency prediction.

Overall, these results clearly verify the effectiveness of all important design features in SalGradNet.

6 Conclusion

In this work, a new fully convolutional network, SalGradNet, for video saliency prediction is proposed. SalGradNet takes as input a video clip and predicts the frame-by-frame saliency map by exploiting, for the prediction on each frame, the temporal information extracted from a fixed number of previous frames ($T = 16$). SalGradNet uses a multi-head encoder-decoder architecture: in the encoding path, 3D feature extraction layers simultaneously aggregate spatio-temporal cues from a sequence of T frames. The encoded features are then provided to the conspicuity networks, that act at different points of the encoder to generate 4 different conspicuity maps, each representing spatio-temporal information at different abstraction levels. These maps finally contribute to the

| source: Hollywood2 - target: DHF1K → testing on Hollywood2 | | | | |
|---|--------------|--------------|--------------|--------------|
| Model | AUC-J | NSS | CC | SIM |
| No GRL | 0.929 | 3.235 | 0.661 | 0.528 |
| GRL | 0.927 | 3.139 | 0.653 | 0.520 |

| source: Hollywood2 - target: DHF1K → testing on DHF1K | | | | |
|--|--------------|--------------|--------------|--------------|
| Model | AUC-J | NSS | CC | SIM |
| No GRL | 0.892 | 2.466 | 0.444 | 0.337 |
| GRL | 0.891 | 2.461 | 0.444 | 0.338 |

| source: Hollywood2 - target: DHF1K → testing on UCF Sports | | | | |
|---|--------------|--------------|--------------|--------------|
| Model | AUC-J | NSS | CC | SIM |
| No GRL | 0.884 | 2.476 | 0.538 | 0.442 |
| GRL | 0.884 | 2.411 | 0.529 | 0.434 |

Table 7 Domain adaptation with source: Hollywood2, target: DHF1K; evaluation on Hollywood2, DHF1K and UCF Sports. Best results in bold.

| | AUC-J | SIM | NSS | CC |
|-------------------|--------------|--------------|--------------|--------------|
| Baseline (T=8) | 0.895 | 0.340 | 2.466 | 0.449 |
| Baseline (T=16) | 0.895 | 0.342 | 2.588 | 0.467 |
| + Consp-net3 | 0.892 | 0.373 | 2.623 | 0.475 |
| + Consp-net2 | 0.902 | 0.373 | 2.700 | 0.484 |
| + Consp-net1 | 0.904 | 0.378 | 2.743 | 0.491 |
| Full model | 0.904 | 0.394 | 2.780 | 0.491 |

Table 8 Comparison of various SalGradNet (without DA) configurations. The *Baseline* configuration refers to the network in a simple encoder-decoder configuration, i.e., with Conspicuity-net 4 only. The full model includes all four conspicuity networks with multi-head loss on conspicuity and saliency maps, defined in Equation 5, and $T = 16$ input frames.

prediction of the saliency map on the last frame of the processed video.

The designed model outperforms state-of-the-art methods over the standard DHF1K benchmark on most metrics for saliency prediction. This, jointly with the performed ablation studies, demonstrates the effectiveness of the devised conspicuity-based approach. Furthermore, the model is able to generalize well, as showed by the performance obtained on two other datasets, Hollywood2 and UCF-Sports.

In terms of domain adaptation, SalGradNet, when enhanced with hierarchical gradient reversal layers, shows performance comparable to state-of-the-art models trained in a supervised manner. This is remarkable and demonstrates the effectiveness of the proposed model. It should be noted that, in general, domain adaptation performance depends on the datasets employed as source and target, since small datasets with limited variability, such as Hollywood2 and UCF Sports, tend to reduce the advantage that our solution brings when generalizing

to datasets unseen or whose annotations were not used during training.

References

1. Vijay Badrinarayanan, Alex Kendall, and Roberto Cipolla. Segnet: A deep convolutional encoder-decoder architecture for image segmentation. *IEEE transactions on pattern analysis and machine intelligence*, 39(12):2481–2495, 2017.
2. Cagdas Bak, Aysun Kocak, Erkut Erdem, and Aykut Erdem. Spatio-temporal saliency networks for dynamic saliency prediction. *IEEE Transactions on Multimedia*, 20(7):1688–1698, 2017.
3. Loris Bazzani, Hugo Larochelle, and Lorenzo Torresani. Recurrent mixture density network for spatiotemporal visual attention. *arXiv preprint arXiv:1603.08199*, 2016.
4. Zoya Bylinskii, Tilke Judd, Aude Oliva, Antonio Torralba, and Frédo Durand. What do different evaluation metrics tell us about saliency models? *IEEE transactions on pattern analysis and machine intelligence*, 41(3):740–757, 2018.
5. Joao Carreira and Andrew Zisserman. Quo vadis, action recognition? a new model and the kinetics dataset. In *CVPR*, pages 6299–6308, 2017.
6. Yangyu Chen, Weigang Zhang, Shuhui Wang, Liang Li, and Qingming Huang. Saliency-based spatiotemporal attention for video captioning. In *2018 IEEE Fourth International Conference on Multimedia Big Data (BigMM)*, pages 1–8. IEEE, 2018.
7. Marcella Cornia, Lorenzo Baraldi, Giuseppe Serra, and Rita Cucchiara. Predicting human eye fixations via an lstm-based saliency attentive model. *IEEE Transactions on Image Processing*, 27(10):5142–5154, 2018.
8. Alexey Dosovitskiy, Philipp Fischer, Eddy Ilg, Philip Hausser, Caner Hazirbas, Vladimir Golkov, Patrick Van Der Smagt, Daniel Cremers, and Thomas Brox. FlowNet: Learning optical flow with convolutional networks. In *ICCV*, pages 2758–2766, 2015.
9. Richard Droste, Jianbo Jiao, and J Alison Noble. Unified image and video saliency modeling. *arXiv preprint arXiv:2003.05477*, 2020.
10. Yaroslav Ganin and Victor Lempitsky. Unsupervised domain adaptation by backpropagation. *arXiv preprint arXiv:1409.7495*, 2014.
11. Yaroslav Ganin and Victor Lempitsky. Unsupervised domain adaptation by backpropagation. In *ICML*, pages 1180–1189, 2015.
12. Yaroslav Ganin, Evgeniya Ustinova, Hana Ajakan, Pascal Germain, Hugo Larochelle, François Laviolette, Mario Marchand, and Victor Lempitsky. Domain-adversarial training of neural networks. *The Journal of Machine Learning Research*, 17(1):2096–2030, 2016.
13. Ross Girshick. Fast r-cnn. In *ICCV*, pages 1440–1448, 2015.
14. Fahad Fazal Elahi Guraya, Faouzi Alaya Cheikh, Alain Tremeau, Yubing Tong, and Hubert Konik. Predictive saliency maps for surveillance videos. In *2010 Ninth International Symposium on Distributed Computing and Applications to Business, Engineering and Science*, pages 508–513. IEEE, 2010.
15. Jonathan Harel, Christof Koch, and Pietro Perona. Graph-based visual saliency. In *NIPS*, pages 545–552, 2007.

16. Xun Huang, Chengyao Shen, Xavier Boix, and Qi Zhao. Salicon: Reducing the semantic gap in saliency prediction by adapting deep neural networks. In *ICCV*, pages 262–270, 2015.
17. Laurent Itti, Christof Koch, and Ernst Niebur. A model of saliency-based visual attention for rapid scene analysis. *IEEE Transactions on pattern analysis and machine intelligence*, 20(11):1254–1259, 1998.
18. Lai Jiang, Mai Xu, Tie Liu, Minglang Qiao, and Zulin Wang. Deepvs: A deep learning based video saliency prediction approach. In *ECCV*, pages 602–617, 2018.
19. Lai Jiang, Mai Xu, and Zulin Wang. Predicting video saliency with object-to-motion cnn and two-layer convolutional lstm. *arXiv preprint arXiv:1709.06316*, 2017.
20. Meina Kan, Shiguang Shan, and Xilin Chen. Bi-shifting auto-encoder for unsupervised domain adaptation. In *ICCV*, 2015.
21. Will Kay, Joao Carreira, Karen Simonyan, Brian Zhang, Chloe Hillier, Sudheendra Vijayanarasimhan, Fabio Viola, Tim Green, Trevor Back, Paul Natsev, et al. The kinetics human action video dataset. *arXiv preprint arXiv:1705.06950*, 2017.
22. Diederik P Kingma and Jimmy Ba. Adam: A method for stochastic optimization. *arXiv preprint arXiv:1412.6980*, 2014.
23. Christof Koch and Shimon Ullman. Shifts in selective visual attention: towards the underlying neural circuitry. In *Matters of intelligence*, pages 115–141. Springer, 1987.
24. Qiuxia Lai, Wenguan Wang, Hanqiu Sun, and Jianbing Shen. Video saliency prediction using spatiotemporal residual attentive networks. *IEEE Transactions on Image Processing*, 29:1113–1126, 2019.
25. Junnan Li, Yongkang Wong, Qi Zhao, and Mohan S Kankanhalli. Unsupervised learning of view-invariant action representations. In *NIPS*, pages 1254–1264, 2018.
26. Shan Li and MC Lee. Fast visual tracking using motion saliency in video. In *ICASSP*, volume 1, pages I–1073. IEEE, 2007.
27. Mei Kuan Lim, Ven Jyn Kok, Chen Change Loy, and Chee Seng Chan. Crowd saliency detection via global similarity structure. In *2014 22nd International Conference on Pattern Recognition*, pages 3957–3962. IEEE, 2014.
28. Panagiotis Linardos, Eva Mohedano, Juan Jose Nieto, Noel E O’Connor, Xavier Giro-i Nieto, and Kevin McGuinness. Simple vs complex temporal recurrences for video saliency prediction. *arXiv preprint arXiv:1907.01869*, 2019.
29. Mingsheng Long, Yue Cao, Jianmin Wang, and Michael I Jordan. Learning transferable features with deep adaptation networks. *arXiv preprint arXiv:1502.02791*, 2015.
30. Li Lu, Jia He, Zhijie Xu, Yuanping Xu, Chaolong Zhang, Jing Wang, and Jianhua Adu. Crowd behavior understanding through siof feature analysis. In *2017 23rd International Conference on Automation and Computing (ICAC)*, pages 1–6. IEEE, 2017.
31. Marcin Marszałek, Ivan Laptev, and Cordelia Schmid. Actions in context. In *CVPR*, pages 2929–2936. IEEE, 2009.
32. S. Mathe and C. Sminchisescu. Actions in the eye: Dynamic gaze datasets and learnt saliency models for visual recognition. *IEEE Transactions on Pattern Analysis and Machine Intelligence*, 37(7):1408–1424, 2015.
33. Stefan Mathe and Cristian Sminchisescu. Actions in the eye: Dynamic gaze datasets and learnt saliency models for visual recognition. *IEEE transactions on pattern analysis and machine intelligence*, 37(7):1408–1424, 2014.
34. Kyle Min and Jason J Corso. Tased-net: Temporally-aggregating spatial encoder-decoder network for video saliency detection. In *ICCV*, pages 2394–2403, 2019.
35. Tam V Nguyen, Mengdi Xu, Guangyu Gao, Mohan Kankanhalli, Qi Tian, and Shuicheng Yan. Static saliency vs. dynamic saliency: a comparative study. In *ACM MM*, pages 987–996, 2013.
36. Hyeonwoo Noh, Seunghoon Hong, and Bohyung Han. Learning deconvolution network for semantic segmentation. In *ICCV*, pages 1520–1528, 2015.
37. Junting Pan, Cristian Canton Ferrer, Kevin McGuinness, Noel E O’Connor, Jordi Torres, Elisa Sayrol, and Xavier Giro-i Nieto. Salgan: Visual saliency prediction with generative adversarial networks. *arXiv preprint arXiv:1701.01081*, 2017.
38. Junting Pan, Elisa Sayrol, Xavier Giro-i Nieto, Kevin McGuinness, and Noel E. O’Connor. Shallow and deep convolutional networks for saliency prediction. In *CVPR*, 2016.
39. Junting Pan, Elisa Sayrol, Xavier Giro-i Nieto, Kevin McGuinness, and Noel E O’Connor. Shallow and deep convolutional networks for saliency prediction. In *CVPR*, pages 598–606, 2016.
40. Sinno Jialin Pan and Qiang Yang. A survey on transfer learning. *IEEE Transactions on knowledge and data engineering*, 22(10):1345–1359, 2009.
41. Joseph Redmon, Santosh Divvala, Ross Girshick, and Ali Farhadi. You only look once: Unified, real-time object detection. In *CVPR*, pages 779–788, 2016.
42. Olaf Ronneberger, Philipp Fischer, and Thomas Brox. U-net: Convolutional networks for biomedical image segmentation. In *MICCAI*, pages 234–241. Springer, 2015.
43. Mark Sandler, Andrew Howard, Menglong Zhu, Andrey Zhmoginov, and Liang-Chieh Chen. Mobilenetv2: Inverted residuals and linear bottlenecks. In *CVPR*, pages 4510–4520, 2018.
44. Jie Shao, Shaohua Kevin Zhou, and Rama Chellappa. Tracking algorithm using background- foreground motion models and multiple cues [surveillance video applications]. In *ICASSP*, volume 2, pages ii–233. IEEE, 2005.
45. Mohammad Shokri, Ahad Harati, and Kimya Taba. Salient object detection in video using deep non-local neural networks. *arXiv preprint arXiv: 1810.07097*, 2018.
46. Khurram Soomro and Amir R Zamir. Action recognition in realistic sports videos. In *Computer vision in sports*, pages 181–208. Springer, 2014.
47. Baochen Sun and Kate Saenko. Deep coral: Correlation alignment for deep domain adaptation. In *ECCV*, pages 443–450. Springer, 2016.
48. Meijun Sun, Ziqi Zhou, Qinghua Hu, Zheng Wang, and Jianmin Jiang. Sg-fcn: A motion and memory-based deep learning model for video saliency detection. *IEEE transactions on cybernetics*, 49(8):2900–2911, 2018.
49. Yuxing Tang, Josiah Wang, Boyang Gao, Emmanuel Delandrea, Robert Gaizauskas, and Liming Chen. Large scale semi-supervised object detection using visual and semantic knowledge transfer. In *CVPR*, pages 2119–2128, 2016.
50. Du Tran, Lubomir Bourdev, Rob Fergus, Lorenzo Torresani, and Manohar Paluri. Learning spatiotemporal features with 3d convolutional networks. In *ICCV*, pages 4489–4497, 2015.
51. Eric Tzeng, Judy Hoffman, Kate Saenko, and Trevor Darrell. Adversarial discriminative domain adaptation. In *The IEEE Conference on Computer Vision and Pattern Recognition (CVPR)*, 2017.

52. Eric Tzeng, Judy Hoffman, Kate Saenko, and Trevor Darrell. Adversarial discriminative domain adaptation. In *CVPR*, pages 7167–7176, 2017.
53. Huiyun Wang, Youjiang Xu, and Yahong Han. Spotting and aggregating salient regions for video captioning. In *ACM MM*, pages 1519–1526, 2018.
54. Mei Wang and Weihong Deng. Deep visual domain adaptation: A survey. *Neurocomputing*, 312:135–153, 2018.
55. Wenguan Wang, Jianbing Shen, Fang Guo, Ming-Ming Cheng, and Ali Borji. Revisiting video saliency: A large-scale benchmark and a new model. In *CVPR*, 2018.
56. Wenguan Wang, Jianbing Shen, Fang Guo, Ming-Ming Cheng, and Ali Borji. Revisiting video saliency: A large-scale benchmark and a new model. In *CVPR*, pages 4894–4903, 2018.
57. Wenguan Wang, Jianbing Shen, and Ling Shao. Video salient object detection via fully convolutional networks. *IEEE Transactions on Image Processing*, 27(1):38–49, 2017.
58. Xiaolong Wang, Ross Girshick, Abhinav Gupta, and Kaiming He. Non-local neural networks. In *CVPR*, pages 7794–7803, 2018.
59. Jianbing Shen Wenguan Wang. Deep visual attention prediction. *IEEE Transactions on Image Processing*, 2018.
60. Xinyi Wu, Zhenyao Wu, Jinglin Zhang, Lili Ju, and Song Wang. Salsac: A video saliency prediction model with shuffled attentions and correlation-based convlstm. In *AAAI*, pages 12410–12417, 2020.
61. Saining Xie, Chen Sun, Jonathan Huang, Zhuowen Tu, and Kevin Murphy. Rethinking spatiotemporal feature learning: Speed-accuracy trade-offs in video classification. In *ECCV*, pages 305–321, 2018.
62. Tong Yubing, Faouzi Alaya Cheikh, Fahad Fazal Elahi Guraya, Hubert Konik, and Alain Trémeau. A spatiotemporal saliency model for video surveillance. *Cognitive Computation*, 3(1):241–263, 2011.
63. Jing Zhang, Tong Zhang, Yuchao Dai, Mehrtash Harandi, and Richard Hartley. Deep unsupervised saliency detection: A multiple noisy labeling perspective. In *CVPR*, pages 9029–9038, 2018.
64. Yang Zhang, Philip David, and Boqing Gong. Curriculum domain adaptation for semantic segmentation of urban scenes. In *ICCV*, pages 2020–2030, 2017.

Appendices

A Detailed input-output sizes of Conspicuity-nets

| Conspicuity-net 1 | | | | | | |
|----------------------------|---------------------------------|------------|------------|------------------------------------|------------------------------------|-----------------------|
| type | kernel/(stride) | Activation | Batch Norm | Input shape | Output shape | Description |
| Decoder 1 | | | | | | |
| Conv3D | $3 \times 1 \times 1/(2, 1, 1)$ | ReLU | Yes | $192 \times 8 \times 16 \times 24$ | $192 \times 4 \times 16 \times 24$ | temporal convolution |
| Conv3D | $3 \times 1 \times 1/(2, 1, 1)$ | ReLU | Yes | $192 \times 4 \times 16 \times 24$ | $192 \times 2 \times 16 \times 24$ | temporal convolution |
| Conv3D | $3 \times 1 \times 1/(2, 1, 1)$ | ReLU | Yes | $192 \times 2 \times 16 \times 24$ | $192 \times 1 \times 16 \times 24$ | temporal convolution |
| Conv2D | $3 \times 3/(1, 1)$ | ReLU | Yes | $192 \times 16 \times 24$ | $128 \times 16 \times 24$ | |
| SepConv2D | $3 \times 3/(1, 1)$ | ReLU | Yes | $128 \times 16 \times 24$ | $128 \times 16 \times 24$ | |
| Upsample | — | — | — | $128 \times 16 \times 24$ | $128 \times 32 \times 48$ | bilinear |
| Conv2D | $3 \times 3/(1, 1)$ | ReLU | Yes | $128 \times 32 \times 48$ | $64 \times 32 \times 48$ | |
| SepConv2D | $3 \times 3/(1, 1)$ | ReLU | Yes | $64 \times 32 \times 48$ | $64 \times 32 \times 48$ | |
| Upsample | — | — | — | $64 \times 32 \times 48$ | $64 \times 64 \times 96$ | bilinear |
| Conv2D | $3 \times 3/(1, 1)$ | ReLU | Yes | $64 \times 64 \times 96$ | $3 \times 64 \times 96$ | |
| SepConv2D | $3 \times 3/(1, 1)$ | ReLU | Yes | $3 \times 64 \times 96$ | $3 \times 64 \times 96$ | |
| Upsample | — | — | — | $3 \times 64 \times 96$ | $3 \times 128 \times 192$ | bilinear |
| Conv2D | $1 \times 1/(1, 1)$ | Sigmoid | No | $3 \times 128 \times 192$ | $1 \times 128 \times 192$ | |
| Domain adaptation branch 1 | | | | | | |
| GRL | — | | | $192 \times 16 \times 24$ | $192 \times 16 \times 24$ | domain adaptation |
| Feature Reduction block | | | | | | |
| Conv2D | $1 \times 1/(1, 1)$ | ReLU | Yes | $192 \times 16 \times 24$ | $64 \times 16 \times 24$ | channel-reduction |
| Conv2D | $1 \times 1/(1, 1)$ | ReLU | Yes | $64 \times 16 \times 24$ | $32 \times 16 \times 24$ | channel-reduction |
| Conv2D | $1 \times 1/(1, 1)$ | ReLU | Yes | $32 \times 16 \times 24$ | $4 \times 16 \times 24$ | channel-reduction |
| Domain Classification | | | | | | |
| Linear | — | ReLU | Yes | 1536 | 512 | fully connected layer |
| Linear | — | ReLU | Yes | 512 | 128 | fully connected layer |
| Linear | — | ReLU | Yes | 128 | 32 | fully connected layer |
| Linear | — | — | No | 32 | 2 | fully connected layer |

Table 1 Detailed input-output sizes of Conspicuity-net 1

| Conspicuity-net 2 | | | | | | |
|----------------------------|---------------------------------|------------|------------|-----------------------------------|-----------------------------------|-----------------------|
| type | kernel/(stride) | Activation | Batch Norm | Input shape | Output shape | Description |
| Decoder 2 | | | | | | |
| Conv3D | $3 \times 1 \times 1/(2, 1, 1)$ | ReLU | Yes | $480 \times 4 \times 8 \times 12$ | $480 \times 2 \times 8 \times 12$ | temporal convolution |
| Conv3D | $3 \times 1 \times 1/(2, 1, 1)$ | ReLU | Yes | $480 \times 2 \times 8 \times 12$ | $480 \times 1 \times 8 \times 12$ | temporal convolution |
| Conv2D | $3 \times 3/(1, 1)$ | ReLU | Yes | $480 \times 8 \times 12$ | $256 \times 8 \times 12$ | |
| SepConv2D | $3 \times 3/(1, 1)$ | ReLU | Yes | $256 \times 8 \times 12$ | $256 \times 8 \times 12$ | |
| Upsample | — | — | — | $256 \times 8 \times 12$ | $256 \times 16 \times 24$ | bilinear |
| Conv2D | $3 \times 3/(1, 1)$ | ReLU | Yes | $256 \times 16 \times 24$ | $128 \times 16 \times 24$ | |
| SepConv2D | $3 \times 3/(1, 1)$ | ReLU | Yes | $128 \times 16 \times 24$ | $128 \times 16 \times 24$ | |
| Upsample | — | — | — | $128 \times 16 \times 24$ | $128 \times 32 \times 48$ | bilinear |
| Conv2D | $3 \times 3/(1, 1)$ | ReLU | Yes | $128 \times 32 \times 48$ | $64 \times 32 \times 48$ | |
| SepConv2D | $3 \times 3/(1, 1)$ | ReLU | Yes | $64 \times 32 \times 48$ | $64 \times 32 \times 48$ | |
| Upsample | — | — | — | $64 \times 32 \times 48$ | $64 \times 64 \times 96$ | bilinear |
| Conv2D | $3 \times 3/(1, 1)$ | ReLU | Yes | $64 \times 64 \times 96$ | $3 \times 64 \times 96$ | |
| SepConv2D | $3 \times 3/(1, 1)$ | ReLU | Yes | $3 \times 64 \times 96$ | $3 \times 64 \times 96$ | |
| Upsample | — | — | — | $3 \times 64 \times 96$ | $3 \times 128 \times 192$ | bilinear |
| Conv2D | $1 \times 1/(1, 1)$ | Sigmoid | No | $3 \times 128 \times 192$ | $1 \times 128 \times 192$ | |
| Domain adaptation branch 2 | | | | | | |
| GRL | — | | | $480 \times 8 \times 12$ | $480 \times 8 \times 12$ | domain adaptation |
| Feature Reduction block | | | | | | |
| Conv2D | $1 \times 1/(1, 1)$ | ReLU | Yes | $480 \times 8 \times 12$ | $64 \times 8 \times 12$ | channel-reduction |
| Conv2D | $1 \times 1/(1, 1)$ | ReLU | Yes | $64 \times 8 \times 12$ | $4 \times 8 \times 12$ | channel-reduction |
| Domain Classification | | | | | | |
| Linear | — | ReLU | Yes | 384 | 64 | fully connected layer |
| Linear | — | ReLU | Yes | 64 | 16 | fully connected layer |
| Linear | — | — | No | 16 | 2 | fully connected layer |

Table 2 Detailed input-output sizes of Conspicuity-net 2

| Conspicuity-net 3 | | | | | | |
|----------------------------|---------------------------------|------------|------------|----------------------------------|----------------------------------|-----------------------|
| type | kernel/(stride) | Activation | Batch Norm | Input shape | Output shape | Description |
| Decoder 3 | | | | | | |
| Conv3D | $3 \times 1 \times 1/(2, 1, 1)$ | ReLU | Yes | $832 \times 2 \times 4 \times 6$ | $832 \times 1 \times 4 \times 6$ | temporal convolution |
| Conv2D | $3 \times 3/(1, 1)$ | ReLU | Yes | $832 \times 4 \times 6$ | $512 \times 4 \times 6$ | |
| SepConv2D | $3 \times 3/(1, 1)$ | ReLU | Yes | $512 \times 4 \times 6$ | $512 \times 4 \times 6$ | |
| SepConv2D | $3 \times 3/(1, 1)$ | ReLU | Yes | $512 \times 4 \times 6$ | $512 \times 4 \times 6$ | |
| Upsample | — | — | — | $512 \times 4 \times 6$ | $512 \times 8 \times 12$ | bilinear |
| Conv2D | $3 \times 3/(1, 1)$ | ReLU | Yes | $512 \times 8 \times 12$ | $256 \times 8 \times 12$ | |
| SepConv2D | $3 \times 3/(1, 1)$ | ReLU | Yes | $256 \times 8 \times 12$ | $256 \times 8 \times 12$ | |
| SepConv2D | $3 \times 3/(1, 1)$ | ReLU | Yes | $256 \times 8 \times 12$ | $256 \times 8 \times 12$ | |
| Upsample | — | — | — | $256 \times 8 \times 12$ | $256 \times 16 \times 24$ | bilinear |
| Conv2D | $3 \times 3/(1, 1)$ | ReLU | Yes | $256 \times 16 \times 24$ | $128 \times 16 \times 24$ | |
| SepConv2D | $3 \times 3/(1, 1)$ | ReLU | Yes | $128 \times 16 \times 24$ | $128 \times 16 \times 24$ | |
| Upsample | — | — | — | $128 \times 16 \times 24$ | $128 \times 32 \times 48$ | bilinear |
| Conv2D | $3 \times 3/(1, 1)$ | ReLU | Yes | $128 \times 32 \times 48$ | $64 \times 32 \times 48$ | |
| SepConv2D | $3 \times 3/(1, 1)$ | ReLU | Yes | $64 \times 32 \times 48$ | $64 \times 32 \times 48$ | |
| Upsample | — | — | — | $64 \times 32 \times 48$ | $64 \times 64 \times 96$ | bilinear |
| Conv2D | $3 \times 3/(1, 1)$ | ReLU | Yes | $64 \times 64 \times 96$ | $3 \times 64 \times 96$ | |
| SepConv2D | $3 \times 3/(1, 1)$ | ReLU | Yes | $3 \times 64 \times 96$ | $3 \times 64 \times 96$ | |
| Upsample | — | — | — | $3 \times 64 \times 96$ | $3 \times 128 \times 192$ | bilinear |
| Conv2D | $1 \times 1/(1, 1)$ | Sigmoid | No | $3 \times 128 \times 192$ | $1 \times 128 \times 192$ | |
| Domain adaptation branch 3 | | | | | | |
| GRL | — | | | $832 \times 4 \times 6$ | $832 \times 4 \times 6$ | domain adaptation |
| Feature Reduction block | | | | | | |
| Conv2D | $1 \times 1/(1, 1)$ | ReLU | Yes | $832 \times 4 \times 6$ | $128 \times 4 \times 6$ | channel-reduction |
| Conv2D | $1 \times 1/(1, 1)$ | ReLU | Yes | $128 \times 4 \times 6$ | $16 \times 4 \times 6$ | channel-reduction |
| Domain Classification | | | | | | |
| Linear | — | ReLU | Yes | 384 | 64 | fully connected layer |
| Linear | — | ReLU | Yes | 64 | 16 | fully connected layer |
| Linear | — | — | No | 16 | 2 | fully connected layer |

Table 3 Detailed input-output sizes of Conspicuity-net 3

| Conspicuity-net 4 | | | | | | |
|----------------------------|---------------------------------|------------|------------|-----------------------------------|-----------------------------------|-----------------------|
| type | kernel/(stride) | Activation | Batch Norm | Input shape | Output shape | Description |
| Decoder 4 | | | | | | |
| Conv3D | $3 \times 1 \times 1/(2, 1, 1)$ | ReLU | Yes | $1024 \times 2 \times 4 \times 6$ | $1024 \times 1 \times 4 \times 6$ | temporal convolution |
| Conv2D | $3 \times 3/(1, 1)$ | ReLU | Yes | $1024 \times 4 \times 6$ | $512 \times 4 \times 6$ | |
| SepConv2D | $3 \times 3/(1, 1)$ | ReLU | Yes | $512 \times 4 \times 6$ | $512 \times 4 \times 6$ | |
| SepConv2D | $3 \times 3/(1, 1)$ | ReLU | Yes | $512 \times 4 \times 6$ | $512 \times 4 \times 6$ | |
| Upsample | — | — | — | $512 \times 4 \times 6$ | $512 \times 8 \times 12$ | bilinear |
| Conv2D | $3 \times 3/(1, 1)$ | ReLU | Yes | $512 \times 8 \times 12$ | $256 \times 8 \times 12$ | |
| SepConv2D | $3 \times 3/(1, 1)$ | ReLU | Yes | $256 \times 8 \times 12$ | $256 \times 8 \times 12$ | |
| SepConv2D | $3 \times 3/(1, 1)$ | ReLU | Yes | $256 \times 8 \times 12$ | $256 \times 8 \times 12$ | |
| Upsample | — | — | — | $256 \times 8 \times 12$ | $256 \times 16 \times 24$ | bilinear |
| Conv2D | $3 \times 3/(1, 1)$ | ReLU | Yes | $256 \times 16 \times 24$ | $128 \times 16 \times 24$ | |
| SepConv2D | $3 \times 3/(1, 1)$ | ReLU | Yes | $128 \times 16 \times 24$ | $128 \times 16 \times 24$ | |
| Upsample | — | — | — | $128 \times 16 \times 24$ | $128 \times 32 \times 48$ | bilinear |
| Conv2D | $3 \times 3/(1, 1)$ | ReLU | Yes | $128 \times 32 \times 48$ | $64 \times 32 \times 48$ | |
| SepConv2D | $3 \times 3/(1, 1)$ | ReLU | Yes | $64 \times 32 \times 48$ | $64 \times 32 \times 48$ | |
| Upsample | — | — | — | $64 \times 32 \times 48$ | $64 \times 64 \times 96$ | bilinear |
| Conv2D | $3 \times 3/(1, 1)$ | ReLU | Yes | $64 \times 64 \times 96$ | $3 \times 64 \times 96$ | |
| SepConv2D | $3 \times 3/(1, 1)$ | ReLU | Yes | $3 \times 64 \times 96$ | $3 \times 64 \times 96$ | |
| Upsample | — | — | — | $3 \times 64 \times 96$ | $3 \times 128 \times 192$ | bilinear |
| Conv2D | $1 \times 1/(1, 1)$ | Sigmoid | No | $3 \times 128 \times 192$ | $1 \times 128 \times 192$ | |
| Domain adaptation branch 4 | | | | | | |
| GRL | — | | | $1024 \times 4 \times 6$ | $1024 \times 4 \times 6$ | domain adaptation |
| Feature Reduction block | | | | | | |
| Conv2D | $1 \times 1/(1, 1)$ | ReLU | Yes | $1024 \times 4 \times 6$ | $512 \times 4 \times 6$ | channel-reduction |
| Conv2D | $1 \times 1/(1, 1)$ | ReLU | Yes | $512 \times 4 \times 6$ | $64 \times 4 \times 6$ | channel-reduction |
| Conv2D | $1 \times 1/(1, 1)$ | ReLU | Yes | $64 \times 4 \times 6$ | $16 \times 4 \times 6$ | channel-reduction |
| Domain Classification | | | | | | |
| Linear | — | ReLU | Yes | 384 | 64 | fully connected layer |
| Linear | — | ReLU | Yes | 64 | 16 | fully connected layer |
| Linear | — | — | No | 16 | 2 | fully connected layer |

Table 4 Detailed input-output sizes of Conspicuity-net 4